CHAOS
Theory and Applications
in Applied Sciences and Engineering

e-ISSN: 2687-4539
RESEARCH ARTICLE
Vol.7 / No.3 / 2025 / pp.239-252
https://doi.org/10.51537/chaos.1619566

Applications of a New 6D Hyperchaotic System with Hidden Attractors in Secure Communication and Wheeled Mobile Robot Navigation

Michael Kopp [*,1] **and Inna Samuilik** [β,α,2]

[*]Institute for Single Crystals, NAS Ukraine, Nauky Ave. 60, Kharkiv 61072, Ukraine, [β]Institute of Life Sciences and Technologies, Daugavpils University, 13 Vienibas Street, LV-5401 Daugavpils, Latvia, [α]Institute of Applied Mathematics, Riga Technical University, LV-1048 Riga, Latvia.

ABSTRACT This paper introduces a novel six-dimensional (6D) chaotic dynamic system characterized by the absence of equilibrium points and the presence of hidden attractors. The study investigates the properties of this innovative system, including the computation of Lyapunov exponents and the Lyapunov dimension. Through comprehensive computer modeling in Matlab-Simulink, phase portraits of numerous hidden attractors are obtained, providing insight into the system's complex dynamics. To validate the theoretical findings, electronic circuits for the 6D chaotic system were designed and implemented using Multisim software. The circuit simulations exhibit behavior consistent with the Matlab-Simulink models, confirming the reliability of the proposed system's dynamics. The paper further explores the synchronization of two identical 6D hyperchaotic systems using active control techniques. Numerical analyses compare the systems behavior before and after control implementation, demonstrating the effectiveness of the active control method in achieving synchronization. Additionally, the active control approach is applied to chaotic masking and decoding of various signals, highlighting its potential in secure communication applications. We presented a novel application of the proposed 6D system as a source of control input signals for independent navigation of multiple mobile robots, and the paths of robots become unpredictable. We investigated the influence of some external factors on the navigation of a chaotic wheeled mobile robot.

KEYWORDS
Hyperchaotic behavior
Hidden attractors
Computer simulation
Circuit implementation
Active control synchronization
Mobile wheel robot

INTRODUCTION

In recent years, chaos theory has witnessed remarkable advancements, driving its integration into a wide array of engineering disciplines. Applications now span lasers (Mengue *et al.* 2024), power systems (Hunaish *et al.* 2021), oscillators (Shvets and Sirenko 2019), neural and genetic networks (Lin *et al.* 2022; Kozlovska *et al.* 2024), cryptographic systems (Shahna 2023), and memristive systems (Zhou *et al.* 2024). Stochastic approaches to chaotic systems are also widely studied (Contreras-Reyes 2021). The foundation for this progress was laid by Lorenz's seminal discovery of a three-dimensional (3D) chaotic system (Lorenz 1963), which spurred extensive exploration of other chaotic systems. A pivotal milestone in this journey was the introduction of the first four-dimensional hyperchaotic system by Rössler (Rössler 1976), which ignited widespread scientific interest in hyperchaos. Hyperchaotic systems, a subclass of nonlinear dynamic systems, exhibit more intricate behavior than conventional chaotic systems. Characterized by the presence of multiple positive Lyapunov exponents, these systems display richer and more complex dynamics, significantly expanding the possibilities for studying and leveraging chaos in higher-dimensional phase spaces (Sprott 2023).

Chaotic systems are usually classified into two types: self-excited attractors, whose basins of attraction intersect with equilibrium points, and hidden attractors, whose basins do not intersect any equilibrium point (Leonov *et al.* 2015). The discovery of hidden attractors in (Leonov *et al.* 2011) has significant advancements in contemporary nonlinear science, opening new avenues for research. A hallmark of many complex dynamical systems is the phenomenon of multistability, where multiple attractors coexist within the same system. This behavior allows a nonlinear dynamical system to exhibit two or more attractors simultaneously, depending on the initial conditions. Recent findings suggest a strong correlation between the multistability of a system and the presence of hidden attractors. The intricate interplay between coexisting attractors and multistability has garnered considerable attention, with extensive investigations in the literature (Lai *et al.*

Manuscript received: 14 January 2025,
Revised: 16 October 2025,
Accepted: 24 October 2025.

[1]michaelkopp0165@gmail.com
[2]inna.samuilika@rtu.lv (**Corresponding author**)

2017; Bayani *et al.* 2019; Lai *et al.* 2019; Ma *et al.* 2021).

In recent years, there has been a growing interest in developing hyperchaotic models in higher dimensions (Liu *et al.* 2019). The challenge of constructing high-dimensional systems with multiple positive Lyapunov exponents while minimizing the number of terms and maximizing the Kaplan-Yorke dimension represents a promising area for research. A critical consideration in this endeavor is adherence to the simplicity criteria proposed by Sprott (Sprott 2023). Although systems with numerous terms can exhibit highly intricate dynamics, prioritizing simpler systems often facilitates practical implementation. Such streamlined models have demonstrated significant potential in applications including chaos control, synchronization, encryption, and optimization. By striking a balance between complexity and simplicity, researchers can unlock new possibilities for leveraging high-dimensional hyperchaotic systems across diverse domains.

Recent years have seen growing interest in the study of six-dimensional (6D) nonlinear systems, which remain considerably less explored than their lower-dimensional counterparts. Recent reviews of 6D dynamical systems (Al-Azzawi and Al-Obeidi 2021; Al-Obeidi and Al-Azzawi 2022; Michael Kopp and Andrii Kopp 2022; Al-Azzawi and Al-Obeidi 2023; Kopp *et al.* 2023) (see Table 1) with dissipative properties reveal that these systems typically comprise 12 or more terms and often include at least two quadratic nonlinear terms. Previous research (Kopp and Samuilik 2024) presented a 6D dynamical system containing merely 11 terms, representing the most parsimonious formulation documented among existing 6D systems (according to references cited in (Kopp and Samuilik 2024)). Expanding on this work, we propose a novel 6D hyperchaotic system distinguished by its streamlined architecture and minimal number of nonlinear components.

Table 1 Recent 6D dynamical systems reported in the literature

Reference	Total	Nonlinear	tanh	Nature
Al-Azzawi and Al-Obeidi (2021)	17	2	No	Dissipative
Aziz and Al-Azzawi (2022)	13	3	No	Dissipative
Al-Talib and Al-Azzawi (2022)	12	4	No	Dissipative
Al-Obeidi and Al-Azzawi (2022)	17	3	No	Dissipative
Michael Kopp and Andrii Kopp (2022)	17	2	No	Dissipative
Al-Talib and Al-Azzawi (2023)	12	4	No	Dissipative
Al-Azzawi and Al-Obeidi (2023)	17	3	No	Dissipative
Kopp *et al.* (2023)	21	4	No	Dissipative
Khattar *et al.* (2024)	12	4	No	Dissipative
Kopp and Samuilik (2024)	11	4	No	Dissipative
This work	**13**	**2**	**1**	**Dissipative**

Significantly, the existing literature lacks any 6D system incorporating a single conventional nonlinearity based on the hyperbolic tangent function. This function, which has been widely employed in chaotic systems including Hopfield neural networks (HNNs) (Lin *et al.* 2023; Chen *et al.* 2023), presents considerable potential for advancing chaos theory. The integration of this nonlinearity into our proposed system highlights its capacity to enhance understanding of high-dimensional chaotic dynamics and extend the range of practical applications.

This manuscript is organized into the following sections. The Introduction provides an overview of the current state of research on high-dimensional chaotic systems and highlights the motivations behind this study. In Section 2, we present the derivation of a novel 6D hyperchaotic dynamical system using state feedback control. Section 3 explores the dynamic characteristics of the proposed 6D nonlinear system. We analyze fixed points, compute the Lyapunov spectrum, and determine the Lyapunov dimension. A computational model of the system is implemented in the Matlab-Simulink environment to validate its dynamics. In Section 4, we design an electronic circuit for the hyperchaotic chaos generator using the Multisim environment. The circuit's operation is simulated, and the results are compared with those obtained from Matlab-Simulink. Section 5 extends the analysis to the numerical synchronization of two identical 6D hyperchaotic systems using the active control method. Section 6 also discusses practical applications of synchronized chaotic signals in communication, emphasizing chaotic signal masking techniques. In Section 7, we simulate the navigation of a wheeled robot, where control inputs are derived from the system's dynamics. The Conclusions section concludes by summarizing the key findings and implications of this study.

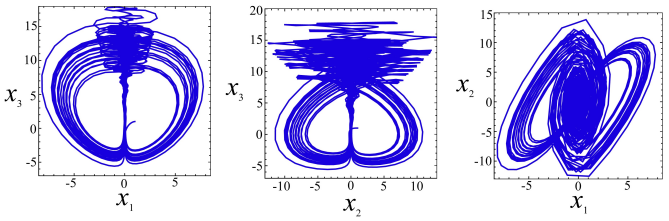

Figure 1 Two-wing butterfly attractors of system (1) for $a = 0.55$ and initial conditions $x_1(0) = x_2(0) = x_3(0) = 1$.

A MATHEMATICAL MODEL OF THE NEW PROPOSED 6D DYNAMIC SYSTEM

Most multidimensional dynamic systems discussed in the literature are commonly derived by extending three-dimensional systems, which serve as the initial framework for observing chaotic behavior. In this section, we introduce a method for constructing a novel six-dimensional dynamical system based on a modified Lorenz system (Elwakil *et al.* 2002), in which the signum function is replaced with the hyperbolic tangent function, as described below:

$$\begin{cases} \dfrac{dx_1}{dt} = a(-x_1 + x_2) \\ \dfrac{dx_2}{dt} = -x_3 \tanh x_1 \\ \dfrac{dx_3}{dt} = |x_1| - 1 \end{cases} \tag{1}$$

The **tanh** function is widely employed in chaotic systems research (e.g., (Lin *et al.* 2022; Zhou *et al.* 2024)) due to its smooth, bounded nature and straightforward circuit implementation. The chaotic attractors of system (1) display a different topology compared to those of the standard Lorenz system. Specifically, in system (1), the chaotic attractors form phase portraits resembling two-winged butterflies (see Figure 1). Following the methodology of Binouse et al. (Binous and Zakia 2008), the Lyapunov exponents (LEs) were calculated as:

$$LE_1 = 0.11096, \quad LE_2 \approx 0, \quad LE_3 = -0.67751.$$

The presence of a positive Lyapunov exponent confirms that system (1) exhibits chaotic behavior. The Kaplan-Yorke (or Lyapunov) dimension is approximately $D_{KY} \approx 2.188$. By introducing a new state variable,x_4, and utilizing the linear feedback control method, we construct a relatively simple four-dimensional (4D) dynamic system with seven terms, described as follows:

$$\begin{cases} \dfrac{dx_1}{dt} = a(-x_1 + x_2) + x_4 \\ \dfrac{dx_2}{dt} = -x_3 \tanh x_1 \\ \dfrac{dx_3}{dt} = |x_1| - 1 \\ \dfrac{dx_4}{dt} = -bx_1 \end{cases} \tag{2}$$

The system (2) demonstrates that the system consists of seven terms, including a nonlinear term involving the hyperbolic tangent $(x_3 \tanh x_1)$, a term with the absolute value function $(|x_1|)$, a constant term $(= 1)$, and four linear terms associated with the state variables x_1, x_2, x_4, interconnected through the positive parameters a and b. For parameter values $a = 0.62$ and $b = 0.55$, with initial conditions $x_1(0) = x_2(0) = x_3(0) = x_4(0) = 1$, the Lyapunov exponents are calculated as:

$$LE_1 = 0.1385,\ LE_2 = 0.0201,\ LE_3 = 0.0076 \approx 0,\ LE_4 = -0.7864.$$

This confirms that system (2) exhibits hyperchaotic behavior, as indicated by the presence of two positive Lyapunov exponents. The Kaplan-Yorke (Lyapunov) dimension is approximately $D_{KY} \approx 3.212$.

To develop a six-dimensional (6D) hyperchaotic model from equation (2), the system's dimensionality must be increased. By applying state feedback control, linear control terms can be introduced for the new state variables x_5 and x_6, in accordance with the equations provided in our paper (Michael Kopp and Andrii Kopp 2022), as follows:

$$\frac{dx_5}{dt} = -x_5 + cx_1 + dx_6,\ \frac{dx_6}{dt} = -x_6 - ex_4 - fx_5, \tag{3}$$

where c, d, e, f are constant defined parameters. By coupling equations (2) and (3), we obtain a new 6D system, which is expressed as follows:

$$\begin{cases} \dfrac{dx_1}{dt} = a(-x_1 + x_2) + x_4 \\ \dfrac{dx_2}{dt} = -x_3 \tanh x_1 \\ \dfrac{dx_3}{dt} = |x_1| - 1 \\ \dfrac{dx_4}{dt} = -bx_1 \\ \dfrac{dx_5}{dt} = -x_5 + cx_1 + dx_6 \\ \dfrac{dx_6}{dt} = -x_6 - ex_4 - fx_5 \end{cases} \tag{4}$$

The system (4) reveals that the system comprises thirteen terms: a nonlinear term involving the hyperbolic tangent $(x_3 \tanh x_1)$, an absolute value term $(|x_1|)$, a constant term $(= 1)$, and ten linear terms related to the state variables x_1, x_2, x_4, x_5, x_6.

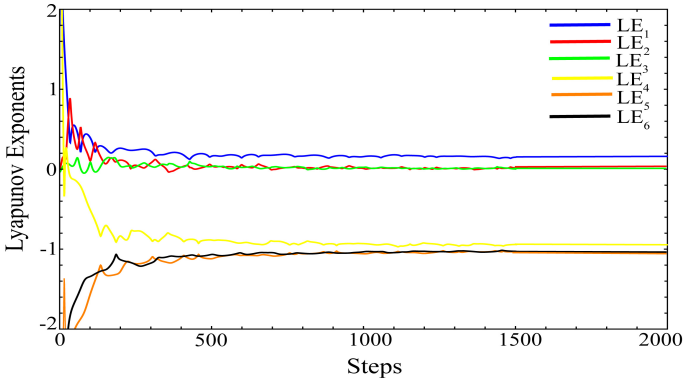

Figure 2 Lyapunov exponents for system (4).

DYNAMICAL ANALYSIS AND MATLAB-SIMULINK MODEL

It is straightforward to verify that system (4) exhibits symmetry about the x_3-axis and remains invariant under the transformation $(x_1, x_2, x_3, x_4, x_5, x_6) \to (-x_1, -x_2, x_3, -x_4, -x_5, -x_6)$. The dissipative nature of system (4) is also evident, which supports the formation of attracting sets, commonly referred to as attractors. The critical points of the system (4) are determined by solving the

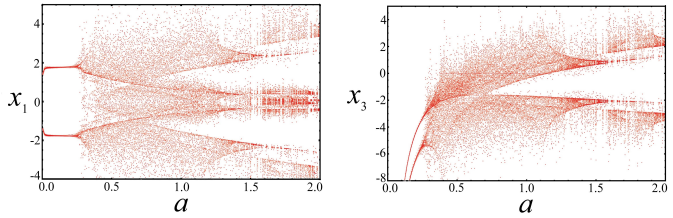

Figure 3 Bifurcation diagrams for x_1 and x_3 components of system (4).

system of equations:

$$\begin{cases} a(-\widetilde{x}_1 + \widetilde{x}_2) + \widetilde{x}_4 = 0 \\ -\widetilde{x}_3 \tanh \widetilde{x}_1 = 0 \\ |\widetilde{x}_1| - 1 = 0 \\ -b\widetilde{x}_1 = 0 \\ -\widetilde{x}_5 + c\widetilde{x}_1 + d\widetilde{x}_6 = 0 \\ -\widetilde{x}_6 - e\widetilde{x}_4 - f\widetilde{x}_5 = 0 \end{cases} \tag{5}$$

We solve the equations (5) under the assumption that a, b, c, d, e, f are non-zero parameters. This leads to $\widetilde{x}_1 = 0$ from the fourth equation. Substituting this value into the third equation results in the contradictory expression $-1 = 0$, which indicates that no equilibrium points exist for the system. As a result, all attractors generated by system (4) are hidden, making standard methods, such as the Shil'nikov theorem, unsuitable for explaining its chaotic dynamics (Silva 1993).

In this study, we show that system (4) exhibits hyperchaotic behavior when the system parameters are chosen as follows:

$$a = 0.83, b = 0.85, c = 8.21, d = 2, e = 24.65, f = 0.1, \tag{6}$$

and the initial conditions (ICs)

$$x_1(0) = x_2(0) = x_3(0) = x_4(0) = x_5(0) = x_6(0) = 1. \tag{7}$$

The Lyapunov exponents of the new system (4) are computed numerically for the parameter values (6) and the initial conditions (7), yielding the following results:

$$LE_1 = 0.1508,\ LE_2 = 0.0170,\ LE_3 = 0.0029 \approx 0,\ LE_4 = -0.9413,$$

$$LE_5 = -1.0324,\ LE_6 = -1.0270. \tag{8}$$

With two positive Lyapunov exponents, LE_1 and LE_2, system (4) is confirmed to exhibit hyperchaotic behavior. Furthermore, the negative sum of the Lyapunov exponents, $\sum_{i=1}^{6} LE_i = -2.83 < 0$, further supports that the hyperchaotic system (4) is dissipative. The Kaplan-Yorke dimension of the proposed hyperchaotic system (4) is calculated as explained in (Frederickson *et al.* 1983):

$$D_{KY} = \xi + \frac{1}{|LE_{\xi+1}|}\sum_{i=1}^{\xi} LE_i = 3 + \frac{0.1707}{0.9413} \approx 3.1813, \tag{9}$$

where ξ is determined from the conditions

$$\sum_{i=1}^{\xi} LE_i > 0 \ \Rightarrow\ \sum_{i=1}^{3} LE_i = 0.1707. \tag{10}$$

Here ξ is the number of first non-negative exponents Lyapunov in the spectrum. The Kaplan-Yorke fractional dimension offers an estimate of the fractal dimension of a strange attractor in a dynamical system. The accuracy of the calculated Lyapunov exponents for the hyperchaotic system (4) with parameter $a = 0.83$ is validated by the fulfillment of the following condition (Singh and Roy 2016):

$$\sum_{i=1}^{6} LE_i = \sum_{i=1}^{6} \frac{\partial}{\partial x_i}\left(\frac{dx_i}{dt}\right) = -2.83\,. \tag{11}$$

Figure 2 depicts the dynamics of the Lyapunov exponents, as described in expression ().

To investigate parameter-dependent dynamics, we constructed bifurcation diagrams by varying parameter $a \in [0, 2]$ while keeping other parameters fixed at $b = 0.85, c = 8.21, d = 2, e = 24.65, f = 0.1$. System (4) was numerically integrated using Mathematica with initial conditions (7). Figure 3 shows bifurcation diagrams plotting the x_1 and x_3 components versus parameter a. The diagrams reveal two symmetric branches of attractors – a lower (left) and an upper (right) branch – that exhibit mirror symmetry with respect to each other. As a increases, both branches undergo period-doubling cascades at identical parameter values, transitioning from periodic oscillations through quasi-periodic states toward chaotic regimes. This symmetry and synchronized bifurcation structure demonstrate the coexistence of dual attractors throughout the parameter range.

It is also valuable to analyze the time series data for the new 6D dynamic system (4) with parameter values (6) and initial conditions (7). In dynamic systems, time series data illustrates how the system evolves over time. By examining the time series, we can observe the behavior of the state variables x_i $(i = 1, 2, 3, 4, 5, 6)$ over time, as shown in Figure 4. The random and complex dependence of the variables x_i on time t is clearly evident. As depicted in Figure 4, the dynamic variables x_2, x_4, x_5, x_6 exceed the power supply limits of the operational amplifiers. To resolve this, the variables in the dynamic system (4) are rescaled as $x_2 = 20X_2$, $x_4 = 20X_4$, $x_5 = 1000X_5$, and $x_6 = 500X_6$, while keeping $x_1 = X_1$ and $x_3 = X_3$ unchanged. This transformation yields the following rescaled hyperchaotic system (4):

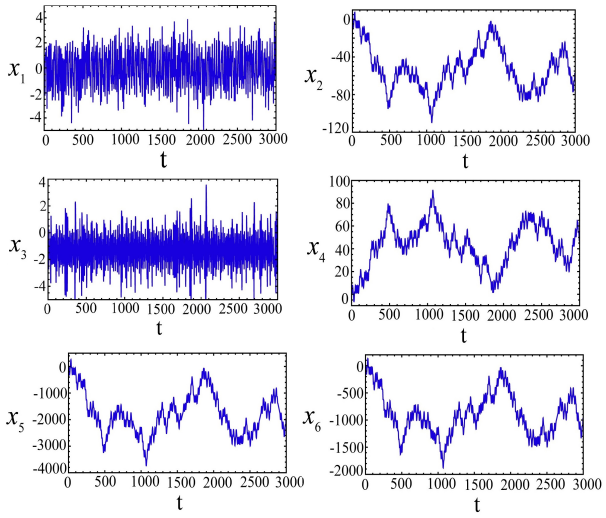

Figure 4 Temporal diagrams for variables $x_1, x_2, x_3, x_4, x_5, x_6$.

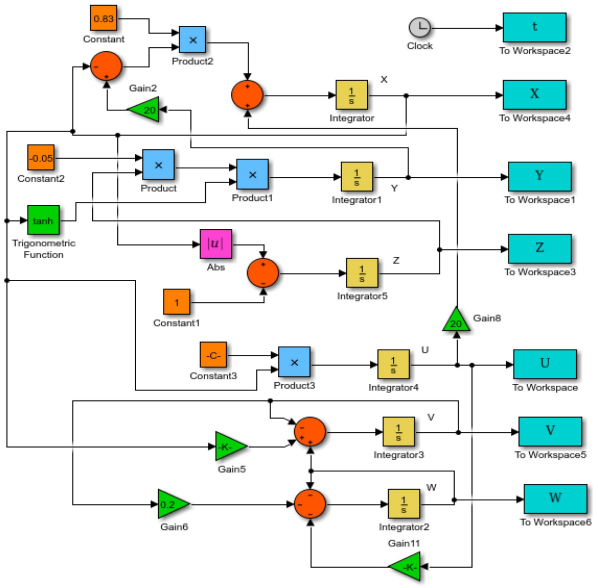

Figure 5 Diagram of the Matlab-Simulink model. In the diagram, the variables X, Y, Z, U, V, W correspond to the variables $X_1, X_2, X_3, X_4, X_5, X_6$ of system (12).

$$\begin{cases} \dfrac{dX_1}{dt} = 0.83(-X_1 + 20X_2) + 20X_4 \\ \dfrac{dX_2}{dt} = -0.05X_3 \tanh X_1 \\ \dfrac{dX_3}{dt} = |X_1| - 1 \\ \dfrac{dX_4}{dt} = -0.0425X_1 \\ \dfrac{dX_5}{dt} = -X_5 + 0.00821X_1 + X_6 \\ \dfrac{dX_6}{dt} = -X_6 - 0.986X_4 - 0.2X_5 \end{cases} \tag{12}$$

For this system, the initial conditions (7) are also transformed as follows:

$$X_1(0) = 1,\ X_2(0) = 0.05,\ X_3(0) = 1,\ X_4(0) = 0.05,$$

$$X_5(0) = 0.001,\ X_6(0) = 0.002. \tag{13}$$

Systems (4) and (12) are equivalent, as the linear transformation merely rescales the variables without affecting the underlying physical properties or dynamics of the nonlinear system. The chaotic attractors of the system of equations (12) were obtained through numerical simulations conducted in MATLAB-Simulink. For this purpose, a MATLAB-Simulink model of the chaotic oscillation generator corresponding to system (12) was utilized. The model consists of interconnected blocks for signal amplification, summation, subtraction, multiplication, integration.

The gain blocks encode the fixed parameter values of system (12). The MATLAB-Simulink model diagram for the 6D hyperchaotic system (12) is presented in Figure 5. Numerical simulations of this model reveal the solutions of the transformed equations (12) with initial conditions (), illustrated as phase portraits of hidden attractors in the X_1X_3, X_2X_3, X_1X_2, X_1X_4, X_2X_5, X_3X_6 planes, as shown in Figure 6. Notably, the range of the dynamic variables X_2, X_4, X_5, X_6 has significantly decreased compared to those shown in Figure 4. This reduction makes it feasible to implement electronic circuits using operational amplifiers, which are constrained to the standard voltage range of -15V to $+15$V.

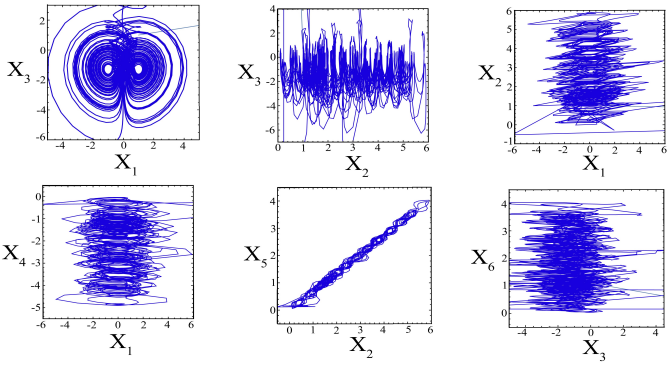

Figure 6 Hidden attractors of the new 6D rescaled system (12) in different planes: a) X_1X_3, b) X_2X_3, c) X_1X_2, d)X_1X_4, e) X_2X_5, f) X_3X_6.

ELECTRONIC CIRCUIT DESIGN

In this section, we implement the theoretical model of the new hyperchaotic system (12) using electronic circuits. Utilizing Kirchhoff's laws for electrical circuits, the electrical analog of the system (12) can be expressed as follows:

$$\begin{cases} C_1\dfrac{dU_1}{d\tau} = -\dfrac{U_1}{R_{11}} + \dfrac{U_2}{R_{12}} + \dfrac{U_4}{R_{13}} \\ C_2\dfrac{dU_2}{d\tau} = -\dfrac{U_3\tanh U_1}{R_{21}K} \\ C_3\dfrac{dU_3}{d\tau} = \dfrac{|U_1|}{R_{31}} - \dfrac{\widetilde{V}_b}{R_{32}} \\ C_4\dfrac{dU_4}{d\tau} = -\dfrac{U_1}{R_{41}} \\ C_5\dfrac{dU_5}{d\tau} = -\dfrac{U_5}{R_{51}} + \dfrac{U_1}{R_{52}} + \dfrac{U_6}{R_{53}} \\ C_6\dfrac{dU_6}{d\tau} = -\dfrac{U_6}{R_{61}} - \dfrac{U_4}{R_{62}} - \dfrac{U_5}{R_{63}} \end{cases} \tag{14}$$

where $\widetilde{V}_b$ is a stable DC voltage source to implement the constant (=1) in a system (14), R_{ij} are resistors $(i, j) = 1, 2, 3, 4, 5, 6$,

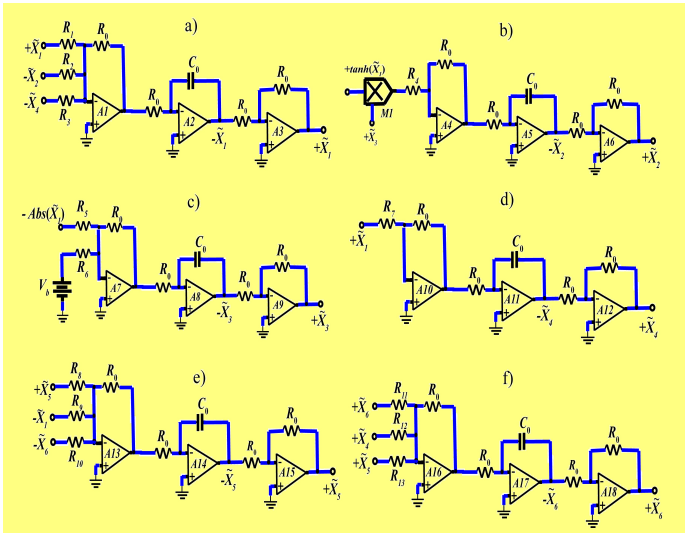

Figure 7 Circuit modules implemented based on a system of equations (15): a) $\widetilde{X}_1$, b) $\widetilde{X}_2$, c) $\widetilde{X}_3$, d) $\widetilde{X}_4$, e) $\widetilde{X}_5$, f) $\widetilde{X}_6$.

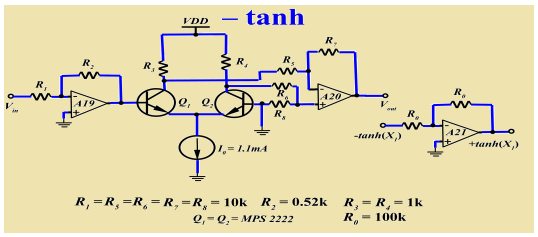

Figure 8 Circuit scheme for realization of hyperbolic tangent function.

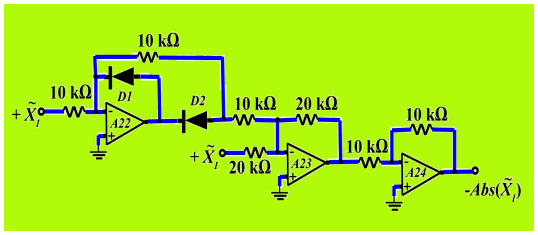

Figure 9 Schematic diagram for the implementation of function absolute value $|\cdot|$.

$U_i(\tau)$ are voltage values, C_i are capacitors, and K is a scaling coefficient for the multiplier. We choose the normalized resistor as $R_0 = 100\text{k}\Omega$ and the normalized capacitor as $C_0 = 1\text{nF}$ (Yu *et al.* 2008). Then the time constant is equal to $t_0 = R_0C_0 = 10^{-4}$s. We rescale the state variables of the system (14) as follows $U_1 = U_0\widetilde{X}_1, U_2 = U_0\widetilde{X}_2, U_3 = U_0\widetilde{X}_3, U_4 = U_0\widetilde{X}_4, U_5 = U_0\widetilde{X}_5, U_6 = U_0\widetilde{X}_6$, $K = U_0K'$, and $\tau = t_0t$. Next, we can write equations (14) in a dimensionless form. After substituting R_0, $C_1 = C_2 = C_3 = C_4 = C_5 = C_6 = C_0$, and $K' = 10$ into (14) and comparing the numerical values with the output voltages of the

system (11), we get the resistor values as follows:

$$\begin{cases} \frac{d\widetilde{X}_1}{dt} = -\frac{100\text{k}}{R_1}\widetilde{X}_1 + \frac{100\text{k}}{R_2}\widetilde{X}_2 + \frac{100\text{k}}{R_3}\widetilde{X}_4 \\ \frac{d\widetilde{X}_2}{dt} = -\frac{100\text{k}}{R_4 \cdot 10}\widetilde{X}_3 \tanh \widetilde{X}_1 \\ \frac{d\widetilde{X}_3}{dt} = \frac{100\text{k}}{R_5}|\widetilde{X}_1| - \frac{100\text{k}}{R_6}V_b \\ \frac{d\widetilde{X}_4}{dt} = -\frac{100\text{k}}{R_7}\widetilde{X}_1 \\ \frac{d\widetilde{X}_5}{dt} = -\frac{100\text{k}}{R_8}\widetilde{X}_5 + \frac{100\text{k}}{R_9}\widetilde{X}_1 + \frac{100\text{k}}{R_{10}}\widetilde{X}_6 \\ \frac{d\widetilde{X}_6}{dt} = -\frac{100\text{k}}{R_{11}}\widetilde{X}_6 - \frac{100\text{k}}{R_{12}}\widetilde{X}_4 - \frac{100\text{k}}{R_{13}}\widetilde{X}_5 \end{cases} \quad (15)$$

where

$$R_1 = 120.48\text{k}\Omega,\ R_2 = 6.024\text{k}\Omega,\ R_3 = 5\text{k}\Omega,\ R_4 = 200\text{k}\Omega,$$

$$R_5 = R_6 = R_8 = R_{10} = R_{11} = 100\text{k}\Omega,$$

$$R_7 = 2.353\text{M}\Omega,\ R_9 = 12.18\text{M}\Omega,\ R_{12} = 101.42\text{k}\Omega,\ R_{13} = 500\text{k}\Omega.$$

Figure 7 illustrates the analog circuit modules corresponding to the equations in system (15). These circuits are built using standard components, including resistors (R), capacitors (C), diodes (D1 and D2, 1N4001), a multiplier (M1, AD633), operational amplifiers (A1-A24, TL084ACN), and a supply voltage of ±15V.

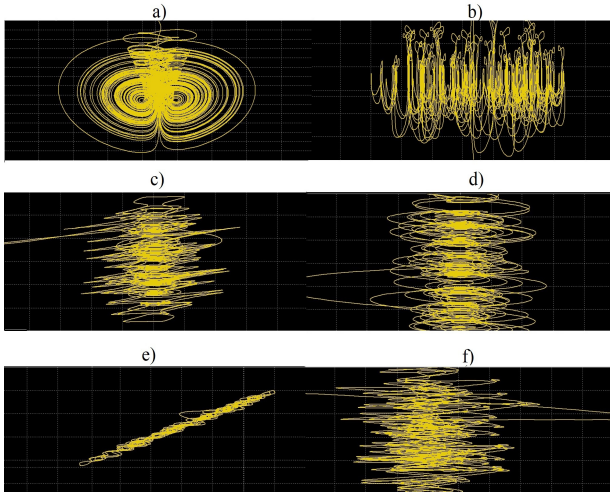

Figure 10 Phase portraits of the new 6D hyperchaotic system as generated in Multisim oscilloscopes: a) $\widetilde{X}_1\widetilde{X}_3$, b) $\widetilde{X}_2\widetilde{X}_3$, c) $\widetilde{X}_1\widetilde{X}_2$, d) $\widetilde{X}_1\widetilde{X}_4$, e) $\widetilde{X}_2\widetilde{X}_5$, f) $\widetilde{X}_3\widetilde{X}_6$.

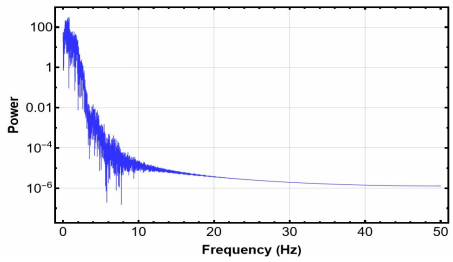

Figure 11 Power spectrum of the chaotic signal X_1 for system (12).

A constant voltage source, $V_b = 1V$, is used to implement a constant value of 1. The electronic circuit designed to realize the hyperbolic tangent function is widely applied in studies involving the dynamics of memristive Hopfield neural networks (see, for example, (Deng *et al.* 2024)). As shown in Figure 8, the equivalent circuit for the inverting hyperbolic tangent function consists of two MPS2222 transistors (Q1 and Q2), two TL084ACN operational amplifiers, a current source ($I_0 = 1.1$mA), and several resistors. The operational amplifiers perform subtraction and input inversion, while the transistors implement the exponential function. The absolute value function ($|\cdot|$) is realized through a conventional electronic circuit that utilizes operational amplifiers (Sedra and Smith 1998), as shown in Figure 9. The phase portraits shown in Figure 10 reveal a remarkable similarity between the results from Matlab-Simulink simulations (Figure 6) and those from Multisim simulations (Figure 10). To assess the frequency characteristics relevant to the TL084 implementation, we performed spectral analysis of the chaotic signals. The power spectrum of the X_1 (see Figure 11) component reveals that the dominant frequency content lies in the range (0.01-10 Hz). The TL084 operational amplifier, with its 3 MHz gain-bandwidth product, slew rate of 13 $V/\mu s$, and low input offset voltage, is well-suited for this relatively low-frequency chaotic dynamics, providing a bandwidth margin exceeding 10^5. This ensures faithful reproduction of the attractor without frequency-dependent distortion. Transistor switching speeds in the tanh implementation circuit are adequate for the system's time scales.For higher-frequency implementations or faster chaotic dynamics, operational amplifiers with higher bandwidth (e.g., AD844 or OPA699) can be used.

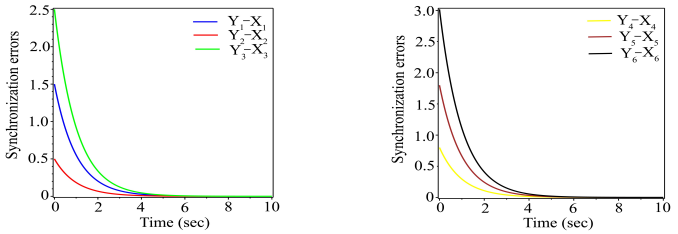

Figure 12 Synchronization error dynamics for 6D hyperchaotic drive and response systems.

CONTROL AND SYNCHRONIZATION TECHNIQUES FOR A NOVEL HYPERCHAOTIC SYSTEM

The development of a new chaotic generator based on 6D nonlinear dynamic equations requires an investigation into its synchronization capabilities to ensure practical applicability. This section presents the use of the active control method (Jung *et al.* 2019; Bhat and Shikha 2019) for synchronizing two identical 6D hyperchaotic systems. We select system (12) as the drive system, while the response system is described as follows:

$$\begin{cases} \frac{dY_1}{dt} = 0.83(-Y_1 + 20Y_2) + 20Y_4 + u_1 \\ \frac{dY_2}{dt} = -0.05Y_3 \tanh Y_1 + u_2 \\ \frac{dY_3}{dt} = |Y_1| - 1 + u_3 \\ \frac{dY_4}{dt} = -0.0425Y_1 + u_4 \\ \frac{dY_5}{dt} = -Y_5 + 0.00821Y_1 + Y_6 + u_5 \\ \frac{dY_6}{dt} = -Y_6 - 0.986Y_4 - 0.2Y_5 + u_6 \end{cases} \quad (16)$$

Here, $Y_1, Y_2, Y_3, Y_4, Y_5, Y_6$ are the state variables, while $u_1, u_2, u_3, u_4, u_5, u_6, u_7$ represent the active controllers to be defined later. The objective is to achieve synchronization between the drive and response systems despite different initial conditions. The state error for each variable is defined as $e_i(t) = Y_i(t) - X_i(t)$, where $i = 1, 2, 3, 4, 5, 6$. By subtracting the drive system (12) from the response system (16), we derive the following error system:

$$\begin{cases} \dot{e}_1 = 0.83(-e_1 + 20e_2) + 20e_4 + u_1 \\ \dot{e}_2 = -0.05(Y_3 \tanh Y_1 - X_3 \tanh X_1) + u_2 \\ \dot{e}_3 = |Y_1| - |X_1| + u_3 \\ \dot{e}_4 = -0.0425e_1 + u_4 \\ \dot{e}_5 = -e_5 + 0.00821e_1 + e_6 + u_5 \\ \dot{e}_6 = -e_6 - 0.986e_4 - 0.2e_5 + u_6 \end{cases} \tag{17}$$

To achieve synchronization of the novel 6D hyperchaotic systems, the next step is to define active control functions that ensure the error system reaches asymptotic stability. The following active control functions have been selected:

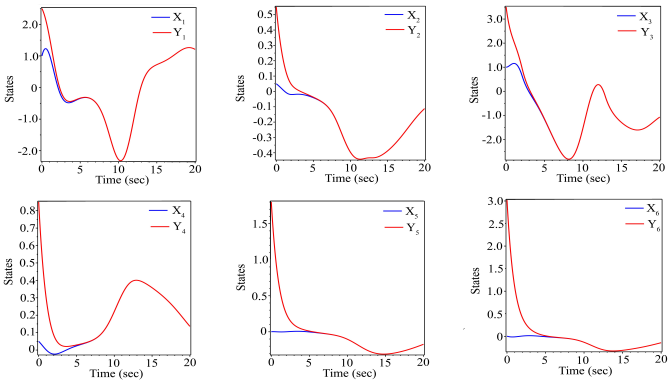

Figure 13 Synchronization of state variables for 6D hyperchaotic drive-response systems.

$$\begin{cases} u_1 = -e_1 + 0.83(e_1 - 20e_2) - 20e_4 \\ u_2 = -e_2 + 0.05(Y_3 \tanh Y_1 - X_3 \tanh X_1) \\ u_3 = -e_3 - (|Y_1| - |X_1|) \\ u_4 = -e_4 + 0.0425e_1 \\ u_5 = -e_6 - 0.00821e_1 \\ u_6 = 0.986e_4 + 0.2e_5 \end{cases} \tag{18}$$

Using the expressions for the active control functions, we derive the dynamic equations of the error system, which are given as follows:

$$\begin{cases} \dot{e}_1 = -e_1 \\ \dot{e}_2 = -e_2 \\ \dot{e}_3 = -e_3 \\ \dot{e}_4 = -e_4 \\ \dot{e}_5 = -e_5 \\ \dot{e}_6 = -e_6 \end{cases} \tag{19}$$

Thus, the application of the proposed active control functions (18) reduced the error system to a linear form. For convenience, we

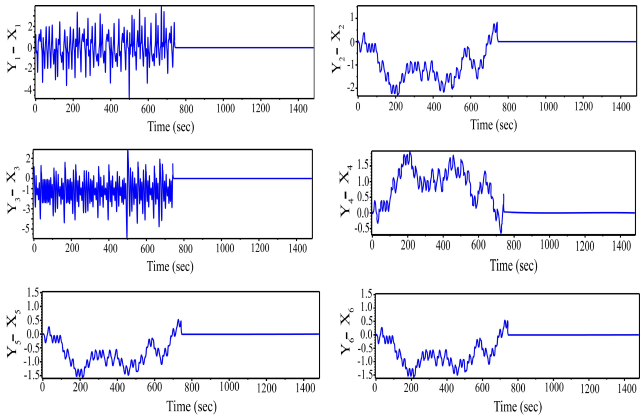

Figure 14 Time evolution of synchronization errors with controller activation and deactivation.

express (19) in matrix form as follows:

$$\begin{vmatrix} \dot{e}_1 \\ \dot{e}_2 \\ \dot{e}_3 \\ \dot{e}_4 \\ \dot{e}_5 \\ \dot{e}_6 \end{vmatrix} = \begin{vmatrix} -1 & 0 & 0 & 0 & 0 & 0 \\ 0 & -1 & 0 & 0 & 0 & 0 \\ 0 & 0 & -1 & 0 & 0 & 0 \\ 0 & 0 & 0 & -1 & 0 & 0 \\ 0 & 0 & 0 & 0 & -1 & 0 \\ 0 & 0 & 0 & 0 & 0 & -1 \end{vmatrix} \begin{vmatrix} e_1 \\ \dot{e}_2 \\ e_3 \\ e_4 \\ e_5 \\ e_6 \end{vmatrix} \tag{20}$$

A straightforward verification confirms that all eigenvalues of the state matrix (20) are negative. Therefore, based on the Routh-Hurwitz criterion, the error system is stable, guaranteeing synchronization between the drive system (12) and the response system (16).

To numerically verify synchronization, we utilized the nonlinear equations (12) and (16. The initial conditions for the drive system (12) were set as follows:

$$X_1(0) = 1,\ X_2(0) = 0.05,\ X_3(0) = 1,\ X_4(0) = 0.05,$$
$$X_5(0) = 0.001,\ X_6(0) = 0.002, \tag{21}$$

and the response system was initialized with:

$$Y_1(0) = 1.5,\ Y_2(0) = 1.55,\ Y_3(0) = 2.5,\ Y_4(0) = 1.55,$$
$$Y_5(0) = 1.501,\ Y_6(0) = 1.502\,. \tag{22}$$

The error curves shown in Figure 12 demonstrate the synchronization process between the drive and response systems, with synchronization errors e_i exponentially converging to zero over time. Moreover, Figure 13 illustrates the state behaviors of both systems, revealing rapid trajectory convergence and confirming the successful synchronization of the hyperchaotic systems.

To enhance the visualization of synchronization via the active control method, we chose a relatively large delay time of $t = 740$ seconds. The active controllers were activated at $t = 740$ seconds, and Figure 14 shows the time evolution of the error states. The simulation results indicate that when the controllers were off $(t < 740s)$, the synchronization errors of the six states exhibited chaotic behavior, indicating the absence of synchronization. However, once the controllers were switched on $(t > 740s)$, all synchronization error states rapidly converged to zero. These results

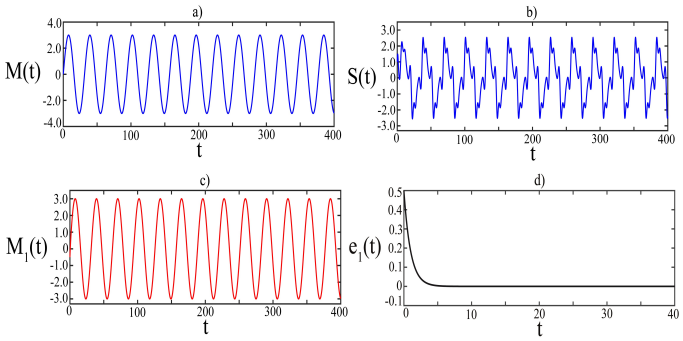

Figure 15 a) Information signal $M(t)$, b) transmitted chaotic signal $S(t)$, c) recovered signal $M_1(t)$, d) error in the information signal $M(t) - M_1(t)$.

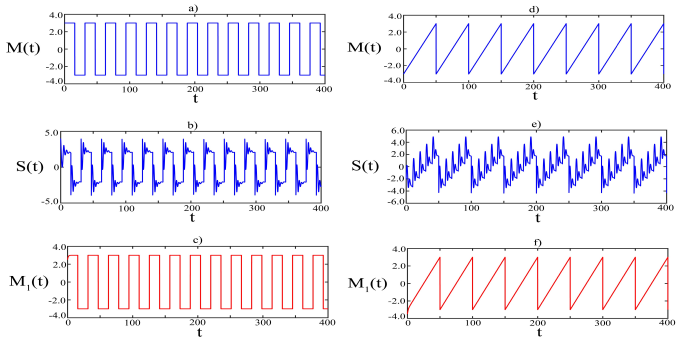

Figure 16 Encryption and decryption of additional message types under ideal transmission: (a)-(c) square-wave input; (d)-(f) sawtooth input.

confirm the effectiveness of the active controllers (18) in synchronizing two identical 6D hyperchaotic systems, even when starting from different initial conditions.

ACTIVE CONTROL METHOD FOR CHAOTIC MASKING AND DECODING OF VARIOUS SIGNALS

In this section, we explore the practical application of the new 6D hyperchaotic system in the field of secure communication (Yang *et al.* 2023; Ozpolat and Gulten 2024). Achieving full synchronization is crucial for the effectiveness of the proposed secure communication technology. We employ an active control method to synchronize two identical 6D hyperchaotic systems that start with different initial conditions. The encrypted signal $S(t)$ is mathematically represented as the sum of the information $M(t)$ and the chaotic signal X_1. Following this, the transmission equation can be readily derived from (11) in the form presented below:

$$\begin{cases} \frac{dX_1}{dt} = 0.83(-S(t) + 20X_2) + 20X_4 \\ \frac{dX_2}{dt} = -0.05X_3 \tanh X_1 \\ \frac{dX_3}{dt} = |X_1| - 1 \\ \frac{dX_4}{dt} = -0.0425S(t) \\ \frac{dX_5}{dt} = -X_5 + 0.00821S(t) + X_6 \\ \frac{dX_6}{dt} = -X_6 - 0.986X_4 - 0.2X_5 \end{cases} \tag{23}$$

For successful decryption of the signal, it is essential that the state variable Y_1 at the receiving end is synchronized with X_1. As a result, the equation for the receiving part is derived from (16) and takes the following form:

$$\begin{cases} \frac{dY_1}{dt} = 0.83(-S_1(t) + 20Y_2) + 20Y_4 + u_1 \\ \frac{dY_2}{dt} = -0.05Y_3 \tanh Y_1 + u_2 \\ \frac{dY_3}{dt} = |Y_1| - 1 + u_3 \\ \frac{dY_4}{dt} = -0.0425S_1(t) + u_4 \\ \frac{dY_5}{dt} = -Y_5 + 0.00821S_1(t) + Y_6 + u_5 \\ \frac{dY_6}{dt} = -Y_6 - 0.986Y_4 - 0.2Y_5 + u_6, \; S_1(t) = M(t) + Y_1 \end{cases} \tag{24}$$

Secure communication under ideal transmission conditions

Clearly, the decrypted signal $M_1(t)$ is computed as follows:

$$M_1(t) = S(t) - Y_1(t) = M(t) + X_1(t) - Y_1(t) = M(t) - e_1.$$

It is evident that as the error e_1 approaches zero, successful signal recovery becomes achievable.

Figure 15 displays the results of a secure communication simulation involving a harmonic information signal represented by $M(t) = 3\sin(0.2t)$ (refer to Figure 15a). After the encryption process, the information signal is transformed into a chaotic state, as illustrated in Figure 15b. This transformation effectively conceals the original signal and ensures secure transmission. In Figure 15c, the information signal is promptly restored to its original form following decryption. Figure 15d illustrates the signal error waveform resulting from the reconstruction of the information signal, which resembles the error observed in the active control synchronization method discussed in the previous subsection. Notably, the error decreases and approaches zero after approximately 5 seconds.

To comprehensively evaluate the encryption and decryption performance of the proposed scheme, additional types of information signals were considered besides the standard sinusoidal waveform. Specifically, three representative test signals were analyzed:
a) square-wave (meander) signal, representing binary or digital information streams;
b) sawtooth waveform, simulating linearly varying, non-stationary data;
c) real data, including short textual or amplitude-modulated messages (e.g., "HELLO CHAOS").
The results obtained for all signal types confirm the universality of the proposed encryption-decryption mechanism. In each case, the original message was efficiently transformed into a complex chaotic waveform, exhibiting no visible resemblance to the original signal in either the time or frequency domains. After decryption, the recovered signals matched their original forms with negligible distortion. Numerical evaluation of the recovery accuracy under ideal transmission conditions showed that the mean absolute reconstruction error remained below 10^{-3}, while the normalized correlation coefficient between the transmitted and recovered signals exceeded 0.999. These values confirm the nearly perfect synchronization and decoding performance of the system in the absence of noise.

Figures 16 and 17 present additional examples of encrypted and decrypted signals obtained for different types of information mes-

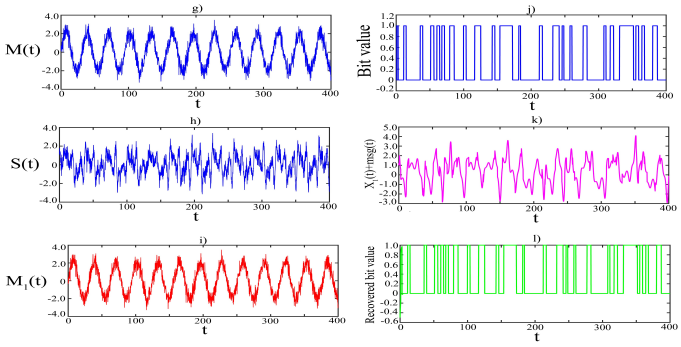

Figure 17 Encryption and decryption of additional message types under ideal transmission conditions: (g)-(i) noisy sinusoidal waveform input; (j)-(l) message "HELLO CHAOS" input.

sages. Figures 16(a-c) correspond to the encryption of rectangular (square-wave) signals, whereas Figures 16(d-f) show the results for sawtooth waveforms. Figures 17(g-i) illustrate the encryption and subsequent recovery of an analog message represented by a noisy sinusoidal waveform,

$$M(t) = A\sin(\omega t) + n(t),$$

where $A = 2$ is the signal amplitude, $\omega = 0.2$ rad/s is the angular frequency, and $n(t)$ denotes additive white Gaussian noise with zero mean and standard deviation $\sigma_n = 0.5$. Such a waveform emulates a realistic analog transmission channel subject to random fluctuations. Figures 17(j-l) demonstrate an example of text transmission, where the message "HELLO CHAOS" is first converted into its ASCII code representation (a binary vector) and then supplied as a stepwise waveform, with each character occupying a fixed time segment. At the receiver side, the decoded signal is converted back from the recovered waveform to binary values, then to ASCII symbols, successfully reconstructing the original text "HELLO CHAOS."

Figures 16 and 17 confirm that, in all tested cases, the proposed chaotic masking and demasking procedure accurately preserves the essential structure of the transmitted information, demonstrating reliable and lossless recovery under ideal (noise-free) transmission conditions.

Testing of secure message transmission under various signal types and channel conditions

In this subsection, we evaluate the performance of the proposed secure communication scheme for different types of messages transmitted through noisy and fading channels. The same types of input signals as in the previous subsection were considered. The following models were used to simulate the communication channel:

- AWGN (Additive White Gaussian Noise) represents additive white Gaussian noise typical of most physical communication channels.
- Channel fading describes temporal variations of the signal amplitude caused by multipath propagation and transient obstructions.

The transmission efficiency was evaluated using the output signal-to-noise ratio (SNR), calculated as

$$\mathrm{SNR}_{\mathrm{out}} = 10\log_{10}\frac{\sum_i s_i^2}{\sum_i (s_i - \hat{s}_i)^2}, \tag{25}$$

where s_i is the original signal and $\hat{s}_i$ is the signal recovered after transmission and decryption. To quantify the preservation of the signal structure, the correlation coefficient between the original and recovered signals was computed as

$$\rho = \frac{\sum_i (s_i - \bar{s})(\hat{s}_i - \bar{\hat{s}})}{\sqrt{\sum_i (s_i - \bar{s})^2 \sum_i (\hat{s}_i - \bar{\hat{s}})^2}}. \tag{26}$$

The results of numerical experiments are summarized in Table 2.

Table 2 Performance of signal recovery for different input types under channel noise simulation. The correlation value indicates the similarity between the original and recovered signals, with 1 corresponding to perfect reconstruction

Signal type	Channel	In SNR (dB)	Out SNR (dB)	Corr.
Sinusoidal	AWGN	20	19.8	0.998
Sinusoidal	AWGN	10	9.5	0.960
Sinusoidal	Fading	15	14.2	0.950
Square-wave	AWGN	20	19.2	0.995
Square-wave	AWGN	10	9.1	0.950
Square-wave	Fading	15	13.8	0.920
Sawtooth	AWGN	20	18.5	0.920
Sawtooth	AWGN	10	8.6	0.850
Sawtooth	Fading	15	12.5	0.820
Real data	AWGN	20	19.6	0.997
Real data	AWGN	12	11.5	0.950
Real data	Fading	15	13.7	0.930

The analysis of the obtained results shows that:

- For sinusoidal and square-wave signals, the correlation remains high (> 0.95) for SNR levels above 10 dB, indicating excellent recovery quality.
- Sawtooth signals are more sensitive to noise, with correlation values decreasing to 0.82-0.92 under moderate noise levels.
- Real data messages can still be correctly decrypted at SNR levels around 12 dB, confirming the practical robustness of the proposed system.
- Under channel fading, short-term SNR drops occur; however, the adaptive synchronization mechanism allows the signal to be accurately reconstructed once the channel exits weak-signal phases.

Thus, comprehensive testing under different signal types and channel models confirms the high efficiency of the proposed secure transmission scheme and its robustness to both noise and fading effects.

CHAOS-BASED TRAJECTORY CONTROL FOR TWO-WHEELED ROBOTS

This section explores the application of a novel hyperchaotic system (12) for controlling a two-wheeled mobile robot. The robot's kinematic model is based on a typical differential drive configuration with two degrees of freedom. It features two active, parallel,

and independently controlled wheels, along with a third passive wheel (Lynch and Park 2017). Output signals from the chaotic system (12) can be utilized as control commands for the mobile robot's motor. By leveraging chaotic algorithms, the robot achieves diverse movement patterns, effectively avoiding previously explored areas and maximizing territorial coverage efficiency. To validate the simulation results of the movement routes, a physical prototype of the robot is usually developed using Arduino microcontrollers (Vaidyanathan *et al.* 2017). The chaotic motion dynamics are implemented via software-based motor control, demonstrating the practical feasibility of the proposed approach. For practical applications, it is also essential to integrate obstacle detection algorithms using data from sensors such as ultrasonic devices. Integrating chaotic dynamics with the motion of a mobile robot requires combining the equations of the chaotic system with the robot's kinematic or dynamic model. The following outlines a step-by-step process for constructing these integrated equations. Let the navigation equations of the mobile robot, based on a kinematic model, be represented by a system of equations (see, for example, (Nwachioma and Perez-Cruz 2021)):

$$\begin{cases} \dfrac{dX}{dt} = v(t)\cos(\Theta(t)) \\ \dfrac{dY}{dt} = v(t)\sin(\Theta(t)) \\ \dfrac{d\Theta}{dt} = w(t) \end{cases} \tag{27}$$

where $\{X(t), Y(t)\}$ is the robot's position on the plane, $v(t) = (v_r(t) + v_l(t))/2$ is the linear velocity of the robot, $v_r(t)$ is linear velocity of the right wheel, $v_l(t)$ is linear velocity of the left wheel, $w(t) = (v_r(t) - v_l(t))/L$ is angular velocity, and L is distance between the two wheels, Θ is the orientation angle. For a differential drive robot, each wheel is independently controlled by a speed signal generated by the chaotic system, thereby enabling a clearer demonstration of the chaotic dynamics.

Let the linear velocities of the right and left wheels, $v_r(t)$ and $v_l(t)$, respectively, be replaced by chaotic signals X_i, corresponding to the phase portraits of hidden attractors shown in Figure 6:

$$\begin{pmatrix} v_r(t) \\ v_l(t) \end{pmatrix} \Rightarrow \begin{pmatrix} X_1 \\ X_3 \end{pmatrix}, \begin{pmatrix} X_2 \\ X_3 \end{pmatrix}, \begin{pmatrix} X_1 \\ X_2 \end{pmatrix}, \begin{pmatrix} X_1 \\ X_4 \end{pmatrix}, \begin{pmatrix} X_2 \\ X_5 \end{pmatrix}, \begin{pmatrix} X_3 \\ X_6 \end{pmatrix}. \tag{28}$$

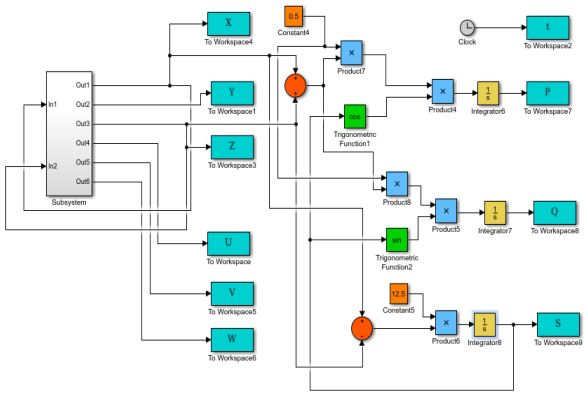

Figure 18 Matlab-Simulink diagram of a chaotic mobile robot based on the system of equations (28). In the diagram, the variables P, Q, S correspond to the variables X, Y, Θ of system (29).

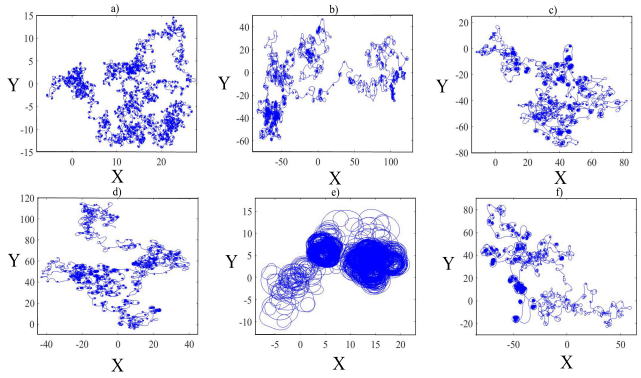

Figure 19 Workspace coverage trajectory of the chaotic mobile robot for system (29) with different chaotic signals on wheels (v_r, v_l): a) (X_1, X_3), b) (X_2, X_3), c) (X_1, X_2), d) (X_1, X_4), e) (X_2, X_5), f) (X_3, X_6)

.

The resulting equations for the chaotic mobile robot are then given by:

$$\begin{cases} \dfrac{dX_1}{dt} = 0.83(-X_1 + 20X_2) + 20X_4 \\ \dfrac{dX_2}{dt} = -0.05X_3 \tanh X_1 \\ \dfrac{dX_3}{dt} = |X_1| - 1 \\ \dfrac{dX_4}{dt} = -0.0425X_1 \\ \dfrac{dX_5}{dt} = -X_5 + 0.00821X_1 + X_6 \\ \dfrac{dX_6}{dt} = -X_6 - 0.986X_4 - 0.2X_5 \\ \dfrac{dX}{dt} = \left(\dfrac{X_n(t) + X_m(t)}{2}\right)\cos(\Theta(t)) \\ \dfrac{dY}{dt} = \left(\dfrac{X_n(t) + X_m(t)}{2}\right)\sin(\Theta(t)) \\ \dfrac{d\Theta}{dt} = \dfrac{X_n(t) - X_m(t)}{L} \end{cases} \tag{29}$$

where $n = (1, 2, 1, 1, 2, 3)$ and $m = (3, 3, 2, 4, 5, 6)$ are indices. Equation system (29) describes the navigation of a mobile robot based on the 6D hyperchaotic system (12), with initial conditions specified in (). We developed a Matlab-Simulink model for an efficient numerical simulation of system (29), as Figure 18 illustrates. The Subsystem in Figure 18 contains the Matlab-Simulink diagram of the hyperchaotic system (12) as in Figure 5. The initial conditions and the value of the parameter L for the kinematic part of equations (29) are defined as follows:

$$X(0) = Y(0) = Z(0) = 0, \quad L = 0.08\,. \tag{30}$$

Figure 19 presents the trajectories of the mobile robot in the $X - Y$ plane of the workspace, obtained from the Matlab-Simulink simulation of the model shown in Figure 18. These trajectories correspond to various chaotic signals applied to the robot's wheels as defined by expression (28). Thus, through the wireless transmission of chaotic signals from multidimensional dynamic systems, such as via Bluetooth or Wi-Fi, it is possible to enable the independent navigation of multiple mobile robots, resulting in unpredictable robot trajectories.

Let us examine how changes in the initial conditions of the kinematic component of equations (29) influence the trajectory of a chaotic mobile robot. For this analysis, we consider the case where

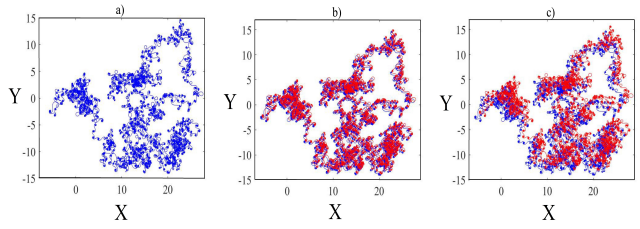

Figure 20 Workspace coverage trajectories of the chaotic mobile robot for system (29) with different ICs.

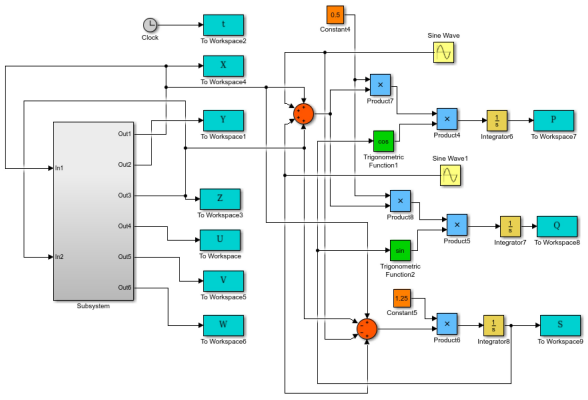

Figure 21 Matlab-Simulink diagram of a mobile robot under impact encrypted signals.

a signal pair (X_1, X_3) is applied to the robot's wheels. The results, obtained using the Matlab-Simulink model, are presented in Figure 20. The trajectories corresponding to the initial conditions defined by (30) are shown in blue in Figures 20a-20c. The trajectories for $(X(0), Y(0), \Theta(0)) = (0.3, 0.3, 0)$ are shown in red in Figure 20b, while those for $(X(0), Y(0), \Theta(0)) = (1, 1, 0)$ are depicted in Figure 20c. As illustrated in Figure 20c, the robot's trajectory in the $X - Y$ plane (highlighted in red) shows significant deviation from the previous trajectory (highlighted in blue) only when the initial conditions undergo a substantial change.

Controlling a mobile robot with combined signals

Consider the scenario where a mixed signal, composed of the additive sum of chaotic and harmonic components, is applied to the mobile robot's right and left wheels. This type of signal, defined as an encrypted signal, was previously introduced in subsection 5.2. The encrypted signal applied to the right wheel can then be expressed in the following form:

$$X_1(t) + A\sin(\omega t), \tag{31}$$

where A and ω are the amplitude and frequency of the useful signal, respectively. The encrypted signal for the left wheel is written similarly, with the harmonic component incorporating a phase shift of $\pi/2$:

$$X_3(t) + A\sin\left(\omega t + \frac{\pi}{2}\right) = X_3(t) + A\cos(\omega t). \tag{32}$$

Figure 21 presents the Matlab-Simulink model used to simulate the trajectory of a mobile robot under the influence of an encrypted signal. Computer simulations of the Matlab-Simulink model (Figure 21) produced the trajectories of the mobile robot in the workspace

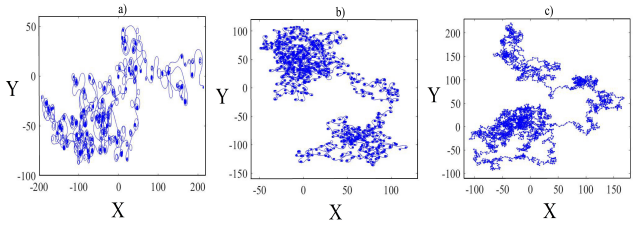

Figure 22 Trajectories of the mobile robot covering the workspace under the influence of a combined signal with varying harmonic signal frequencies: a) $\omega = 0.02$; b) $\omega = 0.2$; c) $\omega = 1$.

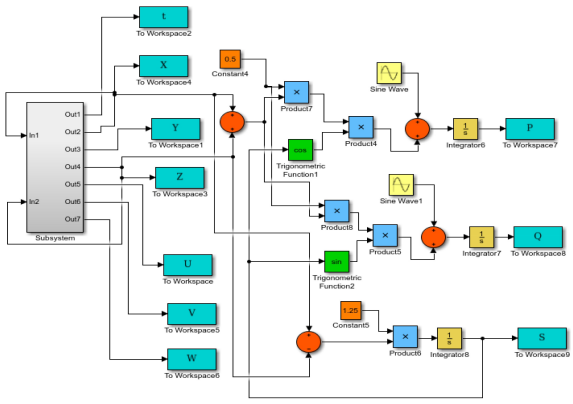

Figure 23 Matlab-Simulink diagram of a mobile robot under impact an external circularly polarized wave.

for various values of the useful signal frequency, as shown in Figure 22. In this scenario, the amplitude of the harmonic signal was kept constant at $A = 10$, with a simulation time of $T = 10000$ s. The simulation results revealed that as the frequency of the harmonic signal increases, the boundaries of the workspace expand, and the robot's trajectory becomes increasingly unpredictable.

The impact of external factors on the chaotic trajectory of a mobile robot

In this subsection, we simulate the effects of external factors – both deterministic and random – on the trajectory of a chaotic mobile robot using the Matlab-Simulink environment. Let us first investigate the effect of an external circularly polarized wave perturbation, which transforms the kinematic equations for the X and Y components in the system (29) into the following form:

$$\frac{dX}{dt} = \left(\frac{X_n(t) + X_m(t)}{2}\right)\cos(\Theta(t)) + A_1\sin\left(\Omega t + \frac{\pi}{2}\right)$$

$$\frac{dY}{dt} = \left(\frac{X_n(t) + X_m(t)}{2}\right)\sin(\Theta(t)) + A_1\sin(\Omega t), \tag{33}$$

where A_1 and Ω are the amplitude and frequency of the circularly polarized wave perturbation.

For simplicity, the amplitude A_1 is set to $A_1 = 1$ during numerical calculations. The Matlab-Simulink diagram from Figure 18, modified to account for the influence of an external circularly polarized wave, is shown in its transformed form in Figure 23. Simulation results of the diagram in Figure 23 indicate that as the frequency of the external wave disturbance decreases, the

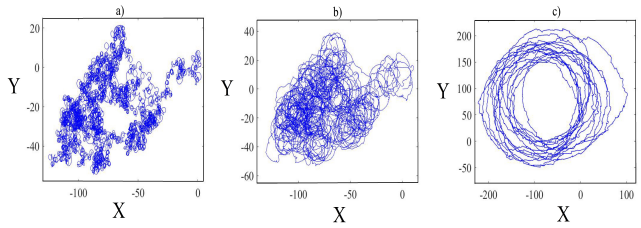

Figure 24 Trajectories of the mobile robot covering the workspace under the influence of an external circularly polarized wave with varying frequencies: a) $\Omega = 1$; b) $\Omega = 0.1$; c) $\Omega = 0.01$.

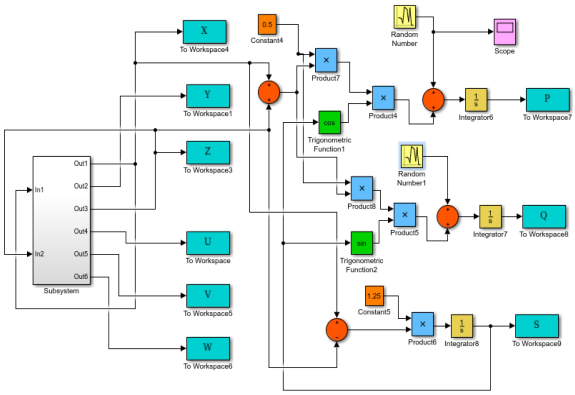

Figure 25 Matlab-Simulink diagram of a mobile robot under impact from external random perturbations.

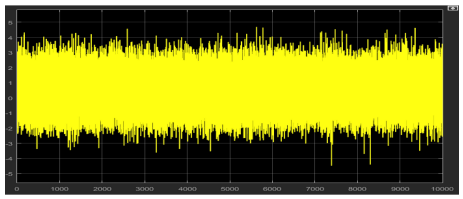

Figure 26 Visual representation of external random perturbations with help from the Scope block.

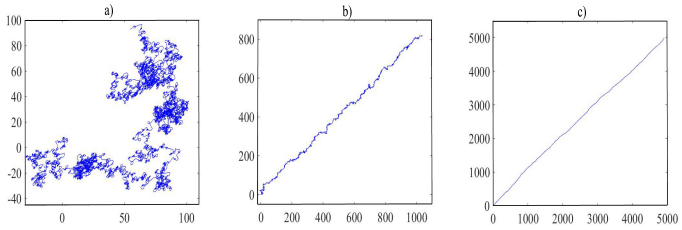

Figure 27 Trajectories of the mobile robot covering the workspace under the influence of an external random perturbations.

boundaries of the workspace expand, and the robot's trajectory becomes more deterministic as shown in Figure 24.

Next, we examine the impact of external random perturbations on the trajectory of a chaotic mobile robot. Assuming the random process follows a Gaussian (normally distributed) signal, the kinematic equations for the X and Y components in system (29) are modified as follows:

$$\begin{aligned} \frac{dX}{dt} &= \left(\frac{X_n(t) + X_m(t)}{2}\right)\cos(\Theta(t)) + \xi(t) \\ \frac{dY}{dt} &= \left(\frac{X_n(t) + X_m(t)}{2}\right)\sin(\Theta(t)) + \xi(t), \end{aligned} \tag{34}$$

where $\xi(t)$ is a Gaussian random process. The Matlab-Simulink diagram for this process is shown in Figure 25.

The Scope block from the diagram in Figure 25 provides a visual representation of the random process as shown in Figure 26. During the simulation of the diagram in Figure 25, we varied the Mean value in the Random Number blocks. The simulation results for different Mean values are shown in Figure 27: a) 0.01, b) 0.1, and c) 0.5. It is observed that as the mean values increase, the working space boundaries of the chaotic mobile robot expand significantly, resulting in a more predictable movement trajectory.

CONCLUSION

In this paper, we introduced a novel 6D hyperchaotic system with 13 terms, incorporating absolute value and hyperbolic tangent functions. This compact 6D system structure has not previously been reported in the literature. A key feature of the system is the absence of equilibrium points, enabling the generation of hidden attractors. All Lyapunov exponents were calculated, with their sum confirming the system's dissipativity through the divergence of its phase flow. For the hyperchaotic behavior, the Kaplan-Yorke dimension was also established. Phase portraits of multiple hidden attractors were obtained through computer modeling of the 6D hyperchaotic system in Matlab-Simulink. Furthermore, an electronic circuit implementation of the system was developed in Multisim 14, with simulation results closely matching those from Matlab-Simulink. Finally, synchronization between two identical 6D hyperchaotic systems was achieved using the active control method. This approach was successfully applied to the chaotic masking and decoding of various signal types, including harmonic, square-wave, sawtooth, and real data signals, demonstrating reliable and secure communication performance under different channel conditions.

The Matlab-Simulink models developed for a chaotic mobile robot based on a novel 6D dynamic system demonstrate potential for a wide range of engineering applications. Simulation results reveal that chaotic signals generated by the multidimensional dynamic system can enable independent navigation of multiple mobile robots, which can be applied to tasks such as search operations, firefighting, and patrol missions. Furthermore, we demonstrated that employing a mixed (encrypted) signal enhances control over the robot's trajectory, ensuring more effective and secure navigation. We also investigated the influence of external factors on the kinematics of the chaotic mobile robot, including circularly polarized waves and random disturbances. The results show that increasing the frequency of wave disturbances makes the robot's trajectory more deterministic while significantly expanding the boundaries of its working space. Similarly, an increase in the intensity of random noise also results in an expanded working space and a more predictable movement trajectory.

Future research directions include investigating the influence of non-Gaussian noise (Contreras-Reyes 2021) on both individ-

ual chaotic robot trajectories and collective flocking dynamics in multi-agent robotic systems, with potential applications to robust navigation under uncertainty. Moreover, the newly proposed 6D hyperchaotic system will be further explored for its applications in image encryption and decryption.

Acknowledgments

We thank two anonymous reviewers for their valuable suggestions and comments.

Ethical standard

The authors have no relevant financial or non-financial interests to disclose.

Availability of data and material

Not applicable.

Conflicts of interest

The authors declare that there is no conflict of interest regarding the publication of this paper.

LITERATURE CITED

Al-Azzawi, S. F. and A. S. Al-Obeidi, 2021 Chaos synchronization in a new 6d hyperchaotic system with self-excited attractors and seventeen terms. Asian-European Journal of Mathematics **14**: 14.

Al-Azzawi, S. F. and A. S. Al-Obeidi, 2023 Dynamical analysis and anti-synchronization of a new 6d model with self-excited attractors. Applied Mathematics - A Journal of Chinese Universities **38**: 27–43.

Al-Obeidi, A. S. and S. F. Al-Azzawi, 2022 A novel six-dimensional hyperchaotic system with self-excited attractors and its chaos synchronisation. International Journal of Computing Science and Mathematics **15**: 72–84.

Al-Talib, Z. S. and S. F. Al-Azzawi, 2022 A new simple 6d hyperchaotic system with nonhyperbolic equilibrium and its electronic circuit. In *2022 International Conference on Computer Science and Software Engineering (CSASE)*, pp. 369–374.

Al-Talib, Z. S. and S. F. Al-Azzawi, 2023 A new simple 6d hyperchaotic system with hyperbolic equilibrium and its electronic circuit. Iraqi Journal of Computer Science and Mathematics **4**: 155–166.

Aziz, S. M. and S. F. Al-Azzawi, 2022 A novel simple 6d hyperchaotic system with hidden attractors. In *2022 International Conference on Computer Science and Software Engineering (CSASE)*, pp. 7–12.

Bayani, A., K. Rajagopal, A. J. M. Khalaf, S. Jafari, G. D. Leutcho, *et al.*, 2019 Dynamical analysis of a new multistable chaotic system with hidden attractor: Antimonotonicity, coexisting multiple attractors, and offset boosting. Physics Letters A **383**: 1450–1456.

Bhat, M. A. and Shikha, 2019 Complete synchronisation of nonidentical fractional order hyperchaotic systems using active control. International Journal of Automation and Control **13**: 140–157.

Binous, H. and N. Zakia, 2008 An improved method for lyapunov exponents computation. Wolfram Library Archive.

Chen, C., F. Min, F. Hu, J. Cai, and Y. Zhang, 2023 Analog/digital circuit simplification for hopfield neural network. Chaos, Solitons & Fractals **173**: 113727.

Contreras-Reyes, J. E., 2021 Chaotic systems with asymmetric heavy-tailed noise: Application to 3d attractors. Chaos, Solitons & Fractals **145**: 110820.

Deng, Q., C. Wang, and H. Lin, 2024 Memristive hopfield neural network dynamics with heterogeneous activation functions and its application. Chaos, Solitons & Fractals **178**: 114387.

Elwakil, A. S., S. Ozoguz, and M. P. Kennedy, 2002 Creation of a complex butterfly attractor using a novel lorenz-type system. IEEE Transactions on Circuits and Systems I: Fundamental Theory and Applications **49**: 527–530.

Frederickson, P., J. L. Kaplan, E. D. Yorke, and J. A. Yorke, 1983 The lyapunov dimension of strange attractors. Journal of Differential Equations **49**: 185–207.

Hunaish, A. S., F. R. Tahir, and H. A. Abbood, 2021 Hyperchaos from dtc induction motor drive system. IFAC-PapersOnLine **54**: 81–86.

Jung, W., S. J. Elliot, and J. Cheer, 2019 Local active control of road noise inside a vehicle. Mechanical Systems and Signal Processing **121**: 144–157.

Khattar, D., N. Agrawal, and M. Sirohi, 2024 Qualitative analysis of a new 6d hyper-chaotic system via bifurcation, the poincare notion, and its circuit implementation. Indian Journal of Physics **98**: 259–273.

Kopp, M. I. and I. Samuilik, 2024 A new 6d two-wing hyperchaotic system: Dynamical analysis, circuit design, and synchronization. Chaos Theory and Applications **6**: 273–283.

Kopp, M. I., A. V. Tur, and V. V. Yanovsky, 2023 Chaotic dynamics of magnetic fields generated by thermomagnetic instability in a nonuniformly rotating electrically conductive fluid. Journal of Physical Studies **27**: 2403.

Kozlovska, O., F. Sadyrbaev, and I. Samuilik, 2024 A new 3d chaotic attractor in gene regulatory network. Mathematics **12**: 100.

Lai, Q., A. Akgul, C. Li, G. Xu, and U. Cavusoglu, 2017 A new chaotic system with multiple attractors: Dynamic analysis, circuit realization and s-box design. Entropy **20**: 12.

Lai, Q., C. Chen, X. W. Zhao, J. Kengne, and C. Volos, 2019 Constructing chaotic system with multiple coexisting attractors. IEEE Access **7**: 24051–24056.

Leonov, G. A., N. V. Kuznetsov, and T. N. Mokaev, 2015 Homoclinic orbits, and self-excited and hidden attractors in a lorenz-like system describing convective fluid motion. European Physical Journal Special Topics **224**: 1421–1458.

Leonov, G. A., N. V. Kuznetsov, and V. I. Vagaitsev, 2011 Localization of hidden chia's attractors. Physics Letters A **375**: 2230–2233.

Lin, H., C. Wang, L. Cui, *et al.*, 2022 Hyperchaotic memristive ring neural network and application in medical image encryption. Nonlinear Dynamics **110**: 841–855.

Lin, H., C. Wang, F. Yu, J. Sun, S. Du, *et al.*, 2023 A review of chaotic systems based on memristive hopfield neural networks. Mathematics **11**: 1369.

Liu, L., C. Du, X. Zhang, J. Li, and S. Shi, 2019 Dynamics and entropy analysis for a new 4-d hyperchaotic system with coexisting hidden attractors. Entropy **21**: 287.

Lorenz, E. N., 1963 Deterministic nonperiodic flow. Journal of Atmospheric Sciences **20**: 130–141.

Lynch, K. M. and F. C. Park, 2017 *Modern Robotics Mechanics, Planning, and Control*. Cambridge University Press.

Ma, C., J. Mou, L. Xiong, S. Banerjee, T. Liu, *et al.*, 2021 Dynamical analysis of a new chaotic system: asymmetric multistability, offset boosting control and circuit realization. Nonlinear Dynamics **103**: 2867–2880.

Mengue, A. D., D. E. Essebe, and B. Z. Essimbi, 2024 High-dimensional hyperchaos and its control in a modified laser system subjected to optical injection. Optical and Quantum Electronics **56**: 1101.

Michael Kopp and Andrii Kopp, 2022 A new 6d chaotic generator: Computer modelling and circuit design. International Journal of Engineering and Technology Innovation **12**: 288–307.

Nazarimehr, F., K. Rajagopal, J. Kengne, S. Jafari, and V. T. Pham, 2018 A new four-dimensional system containing chaotic or hyper-chaotic attractors with no equilibrium, a line of equilibria and unstable equilibria. Chaos, Solitons and Fractals **111**: 108–118.

Nwachioma, C. and H. Perez-Cruz, 2021 Analysis of a new chaotic system, electronic realization and use in navigation of differential drive mobile robot. Chaos, Solitons & Fractals **144**: 110684.

Ozpolat, E. and A. Gulten, 2024 Synchronization and application of a novel hyperchaotic system based on adaptive observers. Applied Sciences **14**: 1311.

Rössler, O. E., 1976 An equation for continuous chaos. Physics Letters A **57**: 397–398.

Sedra, A. S. and K. C. Smith, 1998 *Microelectronics Circuits*. Oxford University Press, New York, fourth edition.

Shahna, K. U., 2023 Novel chaos based cryptosystem using four-dimensional hyper chaotic map with efficient permutation and substitution techniques. Chaos, Solitons & Fractals **170**: 113383.

Shvets, A. and V. Sirenko, 2019 Hyperchaos in oscillating systems with limited excitation. In *Springer Proceedings in Complexity*, pp. 265–273, Springer, Cham.

Silva, C. P., 1993 Shil'nikov's theorem – a tutorial. IEEE Transactions on Circuits and Systems I **40**: 675–682.

Singh, J. P. and B. K. Roy, 2016 The nature of lyapunov exponents is $(+,+,-,-)$. is it a hyperchaotic system? Chaos, Solitons and Fractals **92**: 73–85.

Sprott, J. C., 2023 *Elegant Automation*. World Scientific.

Vaidyanathan, S., A. Sambas, M. Mamat, and M. S. Ws, 2017 A new three-dimensional chaotic system with a hidden attractor, circuit design and application in wireless mobile robot. Archives of Control Sciences **27**: 541–554.

Yang, Y., J. Gao, and H. Imani, 2023 Design, analysis, circuit implementation, and synchronization of a new chaotic system with application to information encryption. AIP Advances **13**: 075116.

Yu, S., W. K. S. Tang, J. Lu, and G. Chen, 2008 Multi-wing butterfly attractors from the modified lorenz systems. In *2008 IEEE International Symposium on Circuits and Systems (ISCAS)*, pp. 768–771, Seattle, WA, USA.

Zhou, X., K. Sun, H. Wang, *et al.*, 2024 Coexisting hyperchaos and multistability in a discrete memristor-coupled bi-neuron model. Nonlinear Dynamics **112**: 9547–9561.

How to cite this article: Kopp, M., and Samuilik, I. Applications of a New 6D Hyperchaotic System with Hidden Attractors in Secure Communication and Wheeled Mobile Robot Navigation. *Chaos Theory and Applications*, 7(3), 239-252, 2025.

Licensing Policy: The published articles in CHTA are licensed under a Creative Commons Attribution-NonCommercial 4.0 International License.